Applied Materials Today 35 (2023) 101929

Contents lists available at ScienceDirect

Applied Materials Today

journal homepage: www.elsevier.com/locate/apmt

Exploring the surface-enhanced Raman scattering (SERS) activity of gold nanostructures embedded around nanogaps at wafer scale: Simulations and experiments

Marta Lafuente [a,b,*], Pablo Muñoz [b], Erwin J.W. Berenschot [a], Roald M. Tiggelaar [c], Arturo Susarrey-Arce [a], Sergio G. Rodrigo [d,f], Lucas J. Kooijman [a], Sonia M. García-Blanco [b], Reyes Mallada [e,f,g], María P. Pina [e,f,g], Niels R. Tas [a,*]

[a] Mesoscale Chemical Systems, MESA+ Institute, University of Twente, P.O. Box 217, AE Enschede 7500, the Netherlands
[b] Integrated Optical Systems, MESA+ Institute, University of Twente, P.O. Box 217, AE Enschede 7500, the Netherlands
[c] NanoLab cleanroom, MESA+ Institute, University of Twente, P.O. Box 217, AE Enschede 7500, the Netherlands
[d] Departamento de Física Aplicada, Facultad de Ciencias, Universidad de Zaragoza, Zaragoza 50009, Spain
[e] Department of Chemical & Environmental Engineering, Edificio I+D+i, Campus Rio Ebro, C/Mariano Esquillor s/n, Zaragoza 50018, Spain
[f] Instituto de Nanociencia y Materiales de Aragón (INMA), CSIC-Universidad de Zaragoza, Zaragoza 50009, Spain
[g] Networking Research Center on Bioengineering, Biomaterials and Nanomedicine, CIBER-BBN, Madrid 28029, Spain

ARTICLE INFO

Keywords:
Ordered nano-wedges
Size-controllable nanogaps
FDTD simulations
Ordered symmetric and asymmetric nanostructures
Ion beam etching (IBE)
Gold sputtering

ABSTRACT

A unique way of converting free space light into a local electromagnetic field in small spaces is via metallic nanostructuring. In this work fabrication, experimental characterization and simulation of surface-enhanced Raman scattering (SERS) active specimens based on Au nanostructures are discussed. We used displacement Talbot lithography (DTL) to fabricate silicon nano-wedge substrates with Au nanostructures embedded around their apices. After the ion beam etching process, a nanogap is introduced between two Au nanostructures templated over nano-wedges, yielding specimens with SERS characteristics. The Au nanostructures and the nanogaps have symmetric and asymmetric configurations with respect to the wedges. With this nanofabrication method, various wafer-scale specimens were fabricated with highly controllable nanogaps with a size in the order of 6 nm for symmetric gaps and 8 nm for asymmetric gaps. SERS characteristics of these specimens were analyzed experimentally by calculating their analytical enhancement factor (AEF). According to finite-difference time-domain (FDTD) simulations, the Raman enhancement arises at the narrow gap due to plasmonic resonances, yielding a maximum AEF of 6.9×10^6. The results highlight the SERS activity of the nanostructures and ultimately comply with reliable substrates for practical applications.

1. Introduction

Raman spectroscopy is a non-destructive technique to study the inelastic scattering of photons caused by matter and can provide rich information about the molecular structure and composition of analytes based on their vibrational fingerprints. However, light has a low probability of being inelastically scattered by a material, thereby making Raman spectroscopy a technique with low sensitivity [1]. This drawback can be overcome by using the Surface Enhanced Raman Scattering (SERS) effect, which increases the Raman signal greatly. SERS is used in multiple biomedical applications, such as diagnosis of degenerative disorders [2] and the presence of virus [3] or genetic diseases [4]. The implementation of SERS in other fields has substantially expanded, e.g., for monitoring and quantification of environmental toxins [5,6], pesticides [7,8], forensic substances [9,10] or nerve agents [11,12].

SERS occurs mainly due to a plasmonic effect in metallic nanostructures [13]. Under light irradiation, a localized collective oscillation of electrons in metallic nanostructures produces a high local electric field, which leads to enhanced Raman scattering from molecules in close contact with the plasmonic nanostructure. SERS can also occur over adsorption sites nearby the electric field enhancement volume. Alongside, localized SERS can be produced in nanometer-sized gaps in

* Corresponding authors.
E-mail addresses: m.lafuenteadiego@utwente.nl, martalaf@unizar.es (M. Lafuente), n.r.tas@utwente.nl (N.R. Tas).

https://doi.org/10.1016/j.apmt.2023.101929
Received 16 June 2023; Received in revised form 30 August 2023; Accepted 7 September 2023
Available online 15 September 2023

between metallic nanostructures, known as SERS "hot-spots", i.e. regions with the highest local electric field.

Plasmonic substrates including metal nanoparticles and lithographically prepared nanostructures are ideal substrates to produce enhanced electric fields. For chemically synthesized nanoparticles, self-assembly on solid supports is one of the most widely applied bottom-up fabrication techniques [14–17]. There, the hot-spots can be found in small free spaces between metal nanoparticles [14,18,19], the assembly of which typically ends randomized in the form of aggregates [20], lacking uniformity and reproducibility that negatively affect the Raman signals [21]. Irreproducibility of Raman signals might be a result of inhomogeneities at the nanogap level. Self-assembly strategies have been adopted widely to alleviate such particle-to-particle nanogap inhomogeneities [22]. Nevertheless, reaching those SERS substrates with highly reproducible and uniform distribution of "hot-spots" at centimetre scale is still a challenge [23–25].

Top-down nanofabrication offers a plethora of options for controlled nanogap fabrication with a wide selection of sizes and geometries, excellent reproducibility, and large-scale uniformity [14,26]. For example, electron beam lithography (EBL) [27] or focus ion beam lithography (FIB) [28] provide maximum control over the nanogap size between nanostructures but suffer from limited scalability. Nanolithography is a flexible and powerful tool that can aid in accelerating the nanofabrication of optical and sensing devices, especially when combined with corner lithography and ion beam etching. A key nanolithographic resource compatible with other nanofabrication methods is displacement Talbot lithography (DTL). This interference nanolithographic method is an emerging patterning technique by means of which ordered nanostructures can be produced with a monochromatic beam over large areas [23,26,29–31]. Likewise, corner lithography combined with the selective anisotropic wet etching of silicon has resulted in the realization of different ordered structures in silicon [32]. Both technologies can ultimately be combined for the top-down nanofabrication of silicon nano-wedges [33]. Such nano-wedges can then render as templates for the formation and size/shape tuning of Au structures with a well-controlled nanogap in-between them. In fact, these nanogaps can be configured symmetrically and asymmetrically with respect to the supporting wedges.

In literature different top-down nanotechnologies have been used for the fabrication of well-ordered, periodic and uniform plasmonic nanostructures and nanogaps. EBL can be used to nanofabricate SERS nanostructures with different geometries: spheres [27], nanostars [34], nanoholes [35] or bimetallic [36] with a resolution up to 10 nm. The main drawback of EBL is it high time consuming and its high costs, for example, fabricating 1 cm^2 with nanostructures of 20 nm requires 111 h [37]. FIB has been used for fabricating nano-antennas [38,39]. Ahmed et al. after a FIB treatment converted a stack of Au (100 nm) – TiO_2 (40 nm) – Au (50 nm) in two symmetric nano-antennas with a length of 35 nm a gap width of 6 nm. Photolithography has been widely used for the fabrication of structures ranging from 500 nm to several microns due to low costs, high uniformity and high throughput [40–42]. Random-ordered silicon nanopillars with a large aspect ratio has been fabricated by means of reactive ion etching (RIE) by controlling the composition of RIE gas mixture [43].

Herein, the SERS activity of Au nanostructures templated over silicon nano-wedges is studied. The nanofabrication of symmetric and asymmetric Au nanostructures was achieved by utilizing ion beam etching of Au films sputter-deposited over silicon nano-wedges. It is important to note that the gap between the symmetric Au nanostructures at the apex of the nano-wedge is also referred to as 'symmetric nanogap', whereas the gap between the asymmetric Au nanostructures is named 'asymmetric nanogap'. Whether or not a symmetric or asymmetric Au nanostructure is formed, depends on the initial thickness of the sputtered gold layer (see Fig. 1). The nano-wedges were realized by a combination of convex corner lithography and anisotropic wet etching. This fabrication method provides size-controllable nanogaps which were used here to go down to $\sim 6 \pm 2$ nm between Au nanostructures. Various such nanogap specimens were prepared to understand the effect of symmetry and asymmetry around nano-wedges. We identified that the etched silicon depth (at the apices of nano-wedges) as well as the Au nanogap width affect the Raman enhancement factor. The simulations conducted with the Finite-Difference Time-Domain (FDTD) method allowed for a better understanding of the electromagnetic (EM) modes responsible for the SERS signal measured over the various Au nanostructure configurations. For the evaluation of their SERS activity, the Analytical Enhancement Factor (AEF) was estimated using rhodamine 6 G (R6G) as the molecular probe.

2. Experimental section

2.1. Fabrication of Au nanostructures embedded on nano-wedges

The SERS-active specimens were fabricated in (100)-oriented silicon (Si) substrates. A simplified summary of the fabrication route followed to produce the SERS-active samples can be found in this section. A detailed explanation of the fabrication process is provided in the supporting information.

Nanolithography by means of DTL and continuation of the top-down fabrication process employing reactive ion etching (RIE) yielded a periodic line pattern defined in stoichiometric silicon nitride (Si_3N_4) (Fig. 2a) [30,31,44,45]. It is noted that this pattern was aligned with the silicon (100) crystal orientation. Etching in potassium hydroxide (KOH)

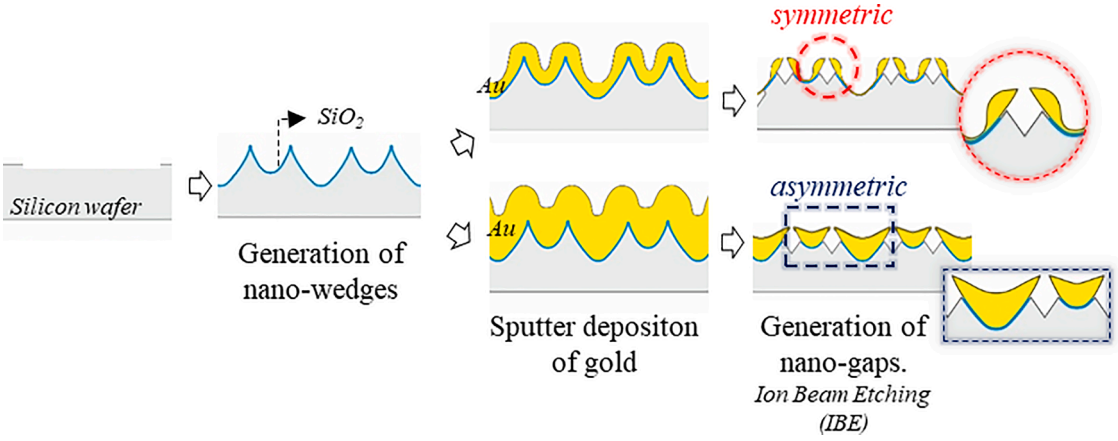

Fig. 1. Schematic overview of the fabrication process for creating symmetric and asymmetric gold nanostructures and, therefore, symmetric and asymmetric nanogaps, respectively.

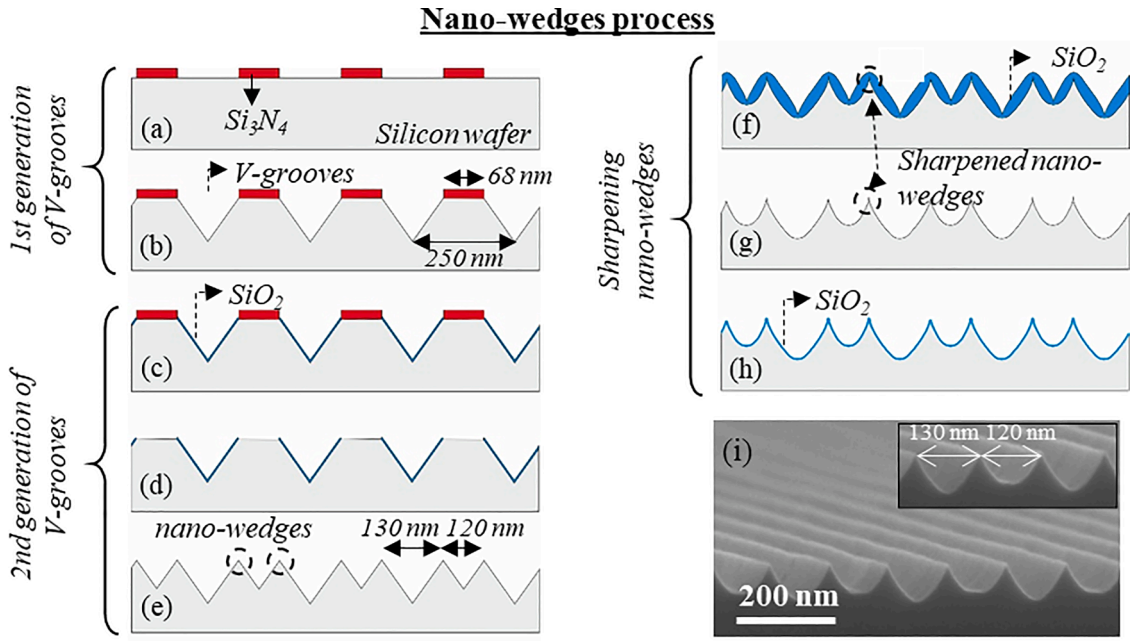

Fig. 2. Schematic representation of the fabrication process of sharpened nano-wedges: (a) Patterning of Si_3N_4 on (100)-Si by DTL and reactive ion etching (RIE), (b) KOH etching of 1st generation of V-grooves using Si_3N_4 as hard mask, (c) LOCOS, (d) Selective removal of Si_3N_4 with H_3PO_4, (e) TMAH etching of 2nd generation of V-grooves using SiO_2 as hard mask, (f) Dry oxidation of nano-wedges, (g) Removal of SiO_2 with HF results in sharpened nano-wedges, (h) Dry oxidation of sharpened nano-wedges. (i) Cross-section SEM image of realized sharpened nano-wedge. The black box shows a magnification of the nano-wedges.

was then applied to generate the first generation of V-shaped nano-grooves (Fig. 2b). Nano-wedges can be realized by removing the flat spacers in-between these nano-grooves. This was accomplished by local oxidation of silicon (LOCOS) (Fig. 2c), followed by selective removal of the Si_3N_4 hard mask with hot phosphoric acid (H_3PO_4) (Fig. 2d). Subsequently, anisotropic etching of the exposed silicon in tetramethyl ammoniumhydroxide (TMAH) was performed, which gave the second generation of V-shaped nano-grooves and hence nano-wedges (Fig. 2e) [46]. The obtained nano-wedges were sharpened using dry oxidation (Fig. 2f) and subsequent removal of the formed silicon dioxide (SiO_2) film using hydrofluoric acid (HF) (Fig. 2g). Prior to Au sputtering, the sharpened nano-wedges were coated with dry SiO_2 (Fig. 2h).

Two different Au thicknesses were sputtered on nano-wedge arrays, i.e., 50 nm and 190 nm (Fig. 3a). Before Au sputtering, a chromium (Cr) layer of 2 nm was sputter-deposited. The Au thickness determines whether size-symmetric or size-asymmetric Au nanostructures will surround the tip of the nano-wedge: size-symmetric implies that the nanostructures present at both sides of each nano-wedge are identical in cross-sectional size (and shape), whereas size-asymmetric means that differently sized Au nanostructures surround the nano-wedges. The Au thickness was reduced with ion beam etching (IBE) until the utmost tip of the nano-wedges were protruding (Fig. 3b). Post to IBE, wet chemical removal of the Cr film from the tip of the nano-wedges was performed, followed by selective removal of the SiO_2 with buffered hydrofluoric acid (BHF) (Fig. 3c). The exposed silicon at the top of each nano-wedge was anisotropically etched in KOH, which yielded openings with a cross-section in the form of rhombic-like cages at the tip of the nano-wedges (Fig. 3d). By means of immersion in BHF and chromium etchant, the SiO_2 and Cr could be removed from within the KOH-etched cage at the tip of the nano-wedge (Fig. 3e). This option was applied to both types of specimen, i.e. with symmetric and asymmetric Au nanostructures. The use of a second Au sputtering step with the aim to reduce the gap between the Au nanostructures was only applied to specimens with asymmetric Au-structures around the nano-wedges (Fig. 3f).

2.2. Materials characterization

High-Resolution scanning electron microscopy (HR-SEM) images of the fabricated nanotextured SERS-active specimens were obtained using a FEI Sirion system. With ImageJ analysis software, five to ten SEM images of each specimen were analyzed to obtain dimensional information about the Au nanostructures around a nanogap, i.e., the gap size as well as the etched silicon depth at the top of a nano-wedge. The uncertainty is expressed in $\pm 1\sigma$. The process of Cr removal was evaluated by preparing a TEM lamella using Focus Ion Beam (FIB) etching (Dual Beam Helios): an asymmetric specimen was cut in a transversal direction and Scanning-transmission electron microscopy (STEM) images were recorded using an FEI Tecnai F30 (see SI Fig. S1).

2.3. Finite-difference time-domain (FDTD) simulations

The plasmonic behavior of nanogap based SERS substrates was simulated using the FDTD method by means of a commercial software package (Lumerical Solutions Inc, FDTD solutions). In the simulations, a model was created for each of the fabricated configurations according to the dimensions as obtained from HR-SEM image analysis. Conformal mesh (mesh accuracy 4) and mesh refinement around the nanogaps were used to define the structure with a minimum mesh size of 0.1 nm. Periodic boundary conditions were considered along the *x*-direction, and the perfectly matched layer (PML) boundary conditions with a steep angle profile were selected along the *y*-direction (it is noted that the *x* and *y*-directions are graphically represented in Fig. 6a). Ideally, PML boundaries would absorb all incident light without creating any back reflection. A plane wave source propagating in the *y*-direction with the electric field parallel to the *x*-direction was employed to excite the system. A convergence test was performed to determine the optimum distance between the SERS nanostructure and the PML boundary conditions in the *y*-direction (2.5 μm). The analysis was performed by considering the "Palik" dispersion curve for Au, silicon and silicon dioxide [47], whereas the refractive index of chromium was taken from the CRC handbook [48].

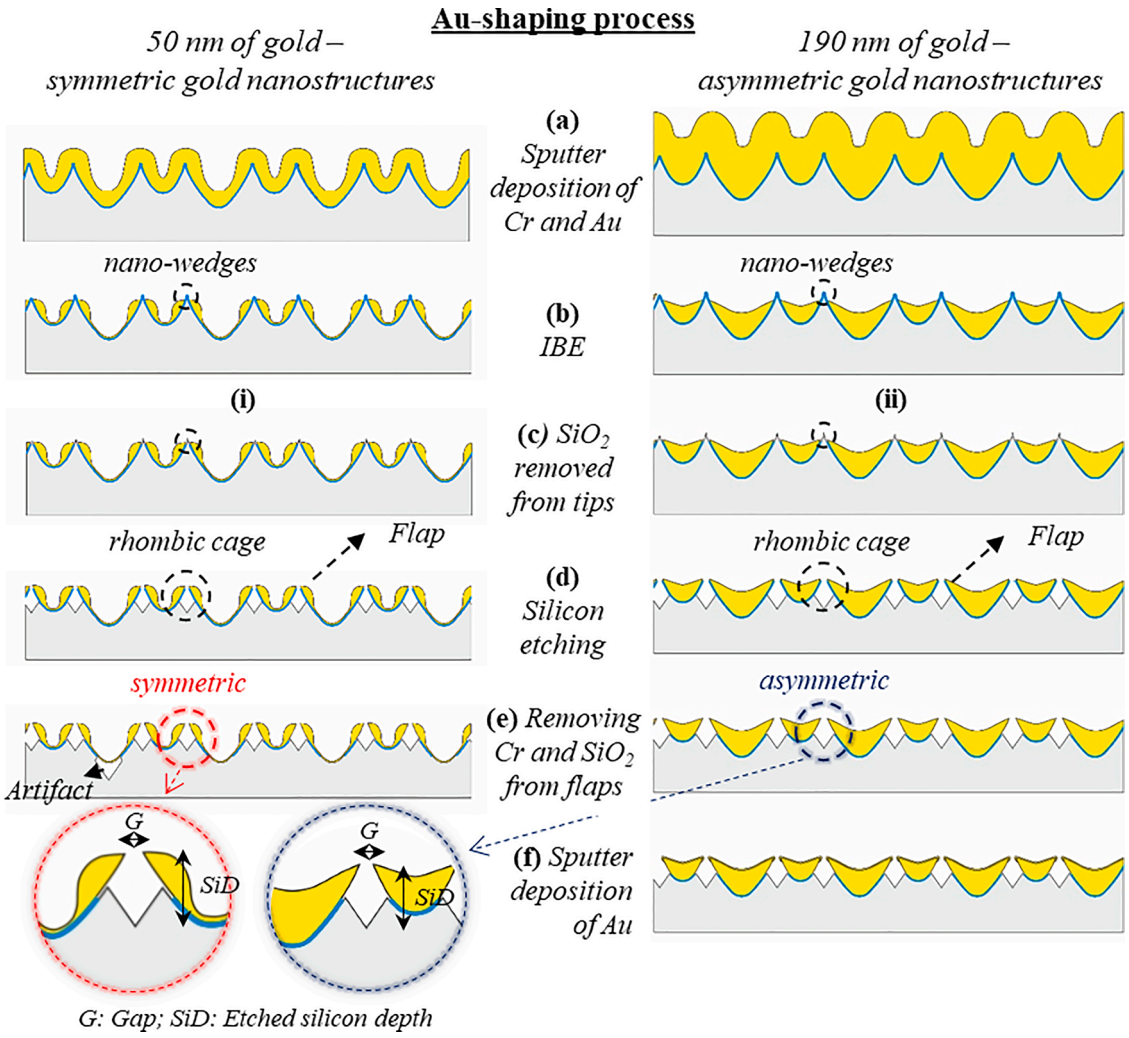

Fig. 3. Schematic representation of the sputtering of Au on oxidized sharpened nano-wedges and further processing into SERS-active specimen: (a) sputtering of Cr/Au, (b) IBE of Au, (c) selective removal of SiO_2 from protruding tips with BHF, (d) KOH etching, (e) selective removal of Cr and SiO_2, (f) sputter deposition of Au to downsize the gap.

2.4. Raman and surface-enhanced Raman scattering (SERS) measurements

An Alpha 300 Raman spectrometer (WITec, Ulm, Germany) was used with a confocal optical microscope (spectral resolution 2 cm^{-1}). Raman-SERS spectra were collected in backscattering configuration. Excitation of the samples was carried out with a 633 nm He-Ne laser, a scattering area of 1.86 μm^2, at room temperature, a laser power of 3 mW, and an acquisition time of 1 s.

SERS substrates (4 mm x 6 mm) were incubated (overnight) in Rhodamine (R6G, Sigma-Aldrich) 1 μM in a vertical position; then, they were rinsed in distilled water and air-dried. Subsequently, on each specimen, five different maps of 50 × 50 μm^2 containing 100 measurement locations were measured. The relative standard deviation (RSD) was the average of these 100 measurements. The Raman intensity of the C—C stretching vibrational mode of R6G at 1510 cm^{-1} was used as a mapping signal. In addition, normal Raman spectra were measured in a 1 mM R6G solution by focusing the laser beam inside the liquid, with 15 mW of power and 50 s collection time. The solution was placed in a polytetrafluoroethylene (PTFE) container of 5 mm × 5 mm × 5 mm (length, width and depth, respectively). In all SERS and Raman spectra, automatic baseline correction, i.e., background subtraction, has been done with WITec Software 2.10.

2.5. Determination of analytical enhancement factor (AEF)

The SERS properties of a plasmonic substrate can be characterized following various methods, the results of which may vary even by a few orders of magnitude [49]. In this work, we use the analytical enhancement factor (AEF). The AEF was calculated according to Eq. (1):

$$AEF = \left(I^*_{SERS} / C_{SERS}\right) / \left(I^*_{Raman} / C_{Raman}\right) \quad (1)$$

Where: C_{Raman} and C_{SERS} are the R6G concentrations during the Raman measurements and SERS conditions, respectively. I^*_{SERS} is the normalized intensity of the R6G molecules on the SERS substrates, and I^*_{Raman} corresponds to the normalized intensity of the R6G molecules measured in the liquid phase (1 mM concentration). In order to perform a fair comparison, both intensities were normalized to laser power and time (cts mW^{-1} s^{-1}).

3. Results & discussion

3.1. Fabrication of Au nanostructures on nano-wedges

The nanofabrication of SERS substrates is based on the sputtering of thin films of Au onto Si etched nano-wedges. The combination of DTL and etching to create nano-wedges onto which Au is sputtered and

further processed into nano-structures is shown in Figs. 2 and 3. Fig. 3 depicts a three-step process that combines DTL, RIE, and anisotropic wet etching of silicon. This process is applied for the top-down fabrication of sharpened nano-wedges. Named as the "nano-wedges process", it produces a template for realization of well-defined Au nanostructures with highly reproducible nanogaps. Fig. 3 shows the subsequent sputter deposition of Au onto these wedges and further nanomachining into two different types of gold nanostructures with defined nanogaps, i.e., size-symmetric and size-asymmetric Au-shapes. This process is referred to as "Au-shaping process". It is important to remember that the symmetry or asymmetry between the Au-nanostructures at the apex of a wedge depends on the initial thickness of the sputtered gold layer (as illustrated in Fig. 3).

We first address the nano-wedges process from Fig. 2. Three main steps constitute this process, which are applied for the nanofabrication of both symmetric as well as asymmetric geometries. The first step starts with the fabrication of the 1st generation of V-grooves in the silicon wafer. Here, a combination of three techniques was employed, i.e., (i) DTL, (ii) RIE, and (iii) anisotropic wet etching of silicon. The DTL-step was used to define a periodic line pattern in a positive photoresist. Subsequently, selective and directional RIE was applied to pattern a 13 nm thick Si_3N_4 layer (Fig. 2a). Then, selective wet etching with KOH produced the first generation of V-shaped nano-grooves, with a pitch of 250 nm and in-between the V-grooves flat spacers of 68 nm wide (Fig. 2b).

The 2nd generation of V-grooves was created by the doubling of the periodicity of the V-grooves. This can be achieved by removing the flat spacers (indicated by the red bars in Fig. 2b) between the 1st generation of V-grooves. Hence, LOCOS was used in combination with an anisotropic wet etching of silicon with TMAH [46]. The aim of the LOCOS-step was to protect the 1st generation of V-grooves during subsequent fabrication steps. LOCOS yielded a SiO_2 layer of 7.9 nm on the Si {111}-walls of the V-grooves, whereas the Si_3N_4 was only slightly oxidized. Then, the Si_3N_4 layer was removed by immersion of the substrate in H_3PO_4. Lastly, the exposed silicon was etched in TMAH for 12 min, resulting in the 2nd generation of V-grooves and hence nano-wedges (Fig. 2e). After this sequence, the widths of the V-grooves were 120 ± 2 nm for the 2nd generation and 130 ± 2 nm for the 1st generation. Post to TMAH etching, the SiO_2 layer was removed with HF.

The third step in Fig. 2, named Sharpening nano-wedges, was applied to obtain smaller gaps between the Au nanostructures. To accomplish this, the substrate was dry oxidized, during which the nano-wedges were sharpened (Fig. 2f) [50]. Afterwards, the SiO_2 film was removed with HF. Finally, in order to avoid the formation of Au-silicide, the sharpened nano-wedges were coated with 3 nm of SiO_2 before Au sputtering (Fig. 2h).

Next, two different Au thicknesses (i.e., 50 nm and 190 nm) were sputtered on nano-wedges to achieve symmetric and asymmetric Au nanogaps (Fig. 3a). The Au thickness was reduced with IBE until the tips of the nano-wedges protruded (Fig. 3b). Note that the thickness of the initially sputtered Au film determined whether the remaining Au-pattern around a nano-wedge was symmetric or asymmetric and the time length of IBE the width of Au nanogap together with the last sputtering step of Au for further finetuning. Hence, the IBE of 50 nm Au yielded equally sized Au-shapes on the left-hand and right-hand side of each wedge (Fig. 3b(i)), whereas IBE of 190 nm Au resulted in differently sized Au-structures at both sides of each nano-wedge (Fig. 3b(ii)). The metallic adhesion layer (i.e., 2 nm Cr) and SiO_2 were removed to gain access to the silicon tip of the nano-wedge (Fig. 3c). The exposed tip was etched in KOH, yielding to a cage with a rhombic-like cross-section at the top of each wedge (Fig. 3d). Applying this KOH-step resulted in a nano-textured SERS-active specimen in which Au adhered with Cr was present on SiO_2 flaps (Fig. 3d).

The described fabrication process can be easily adapted to create multiple variations of SERS-active specimens as shown in Table 1. The slightly adapted process utilizes a shorter immersion in KOH, generating a different depth of the rhombic cages. The other two additional process sequences that were employed concern *i)* removal of the SiO_2 and Cr present at the inside of the KOH-etched feature at the top of the wedges (Fig. 3e) and *ii)* downsizing of the gap between the Au-structures by means of a 2nd sputtering step (Fig. 3f). Table 1 summarizes the typical dimensions and characteristics of the fabricated SERS substrates. Taking into account the cleanroom costs, one specimen costs approximately 45 €.

Table 1
Dimensions and characteristics of nano-textured SERS-active specimens studied in this work (it is noted that '*sym*' and '*asym*' in the sample I.D. refer to symmetry or asymmetry (in size and shape) of the Au-patterns around a wedge). The uncertainty is expressed in ± 1σ.

Sample I. D.	Gap (*G*) [nm]	Etched silicon depth (*SiD*) [nm]	Additional processing
sym1	6 ± 2	0	removal of SiO_2 and Cr
sym2	6 ± 2	13 ± 1	removal of SiO_2 and Cr
sym3	6 ± 2	40 ± 3	removal of SiO_2 and Cr
sym4	6 ± 2	40 ± 3	–
asym1	16 ± 4	100 ± 5	removal of SiO_2 and Cr
asym2	12 ± 3	100 ± 5	removal of SiO_2 and Cr, Au sputtering
asym3	8 ± 3	100 ± 5	removal of SiO_2 and Cr, Au sputtering

Now we turn our attention to the fabricated specimen with symmetric Au nanostructures (named as '*sym*') in Table 1 and SEM images in Fig. 4. From the SEM images, the etched silicon depth was estimated and showed small variations around 13 ± 1 nm or 40 ± 3 nm for a fixed gap of 6 ± 2 nm. For the same structures, the length of the Au flap was 67 ± 7 nm, and the thickness was 16 ± 3 nm. It is worth noting that due to the IBE process, the Au-film in the widest V-groove has become thinner than the gold layer on the sides of the wedges. As a consequence, during the HF-step at which the SiO_2 is removed from the tips of the wedges, HF can also penetrate through the locally thinned (or through defects/holes in the) Au-film and etch the SiO_2. Moreover, some points in the wide V-groove could lead to the defective etched silicon underneath the Au, yielding "artifacts" as indicated with a red arrow in Fig. 4. It is noted that these artifacts are not considered in our numerical simulations.

Figs. 5a-5f show HR-SEM images of the asymmetric Au nanogaps (named as '*asym*'). The nanogap size was tuned between 8 and 16 nm with an additional Au sputtering step, as illustrated in Fig. 3f. The SEM images in Fig. 5 reveal the nanogap reduction as a function of the sputtered-deposited additional Au layer. The structures shown in Figs. 5a & 5d (sample 'asym1') are employed as control with the widest nanogap of 16 ± 4 nm, while the structure in Figs. 5b & 5e (sample 'asym2') and Figs. 5c & 5f (sample 'asym3') confirm nanogap reduction down to 12 ± 3 and 8 ± 3 nm, respectively. For a clear comparison between '*sym*' and '*asym*', consult Table 1 and the histograms in Figs. 5g-5i. The widths of the largest parts of asymmetric nanostructures were measured and found to be 126 ± 3 nm (asym1), 131 ± 5 nm (asym2) and 136 ± 2 nm (asym3), respectively (Fig. 4). The widths of the smallest parts were 91 ± 3 nm, 95 ± 3 nm and 98 ± 3 nm, respectively. The etched silicon depth was 100 ± 5 nm for all asymmetric specimens.

Finally, we verified that the Cr layer was removed, as explained in Fig. 2e, i.e., from the Au nanostructure, by STEM analysis (see Figure S1). The chemical analysis confirmed that Cr was completely removed from the Au "flaps", whereas it remained at the interface between Au and silicon. The STEM images also evidence the absence of Au inside the rhombic cages after the second (optional) gold sputtering step.

To summarize, our nanofabrication process, which combines the fabrication of nano-wedges in silicon with Au sputter-deposition, allows for the fabrication of robust and highly uniform SERS substrates at wafer-scale. In addition, upon performing slight modifications, various SERS nanostructures can be fabricated with well-controlled gaps and, therefore, hot-spot distribution.

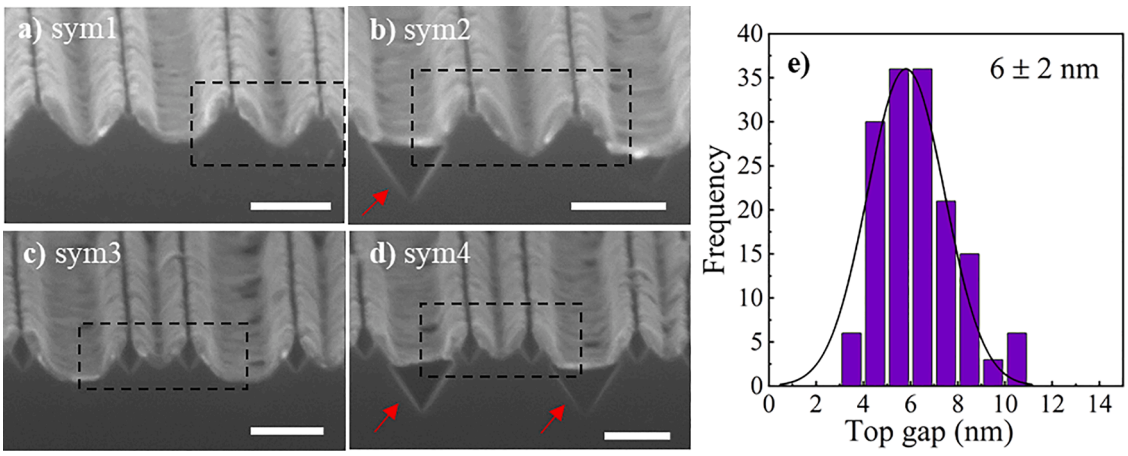

Fig. 4. Cross-sectional SEM images of realized wedge-based samples with symmetric Au nanostructures: a) sym1; b) sym2; c) sym3 and d) sym4. For more details about the sample, see Table 1. The scale bar is 100 nm. The black box shows the unit cells used in the simulations. Red arrows indicate the mentioned artifacts. e) Corresponding size distribution histogram (N>150) of the gap as estimated from 3 different top-view HR-SEM images.

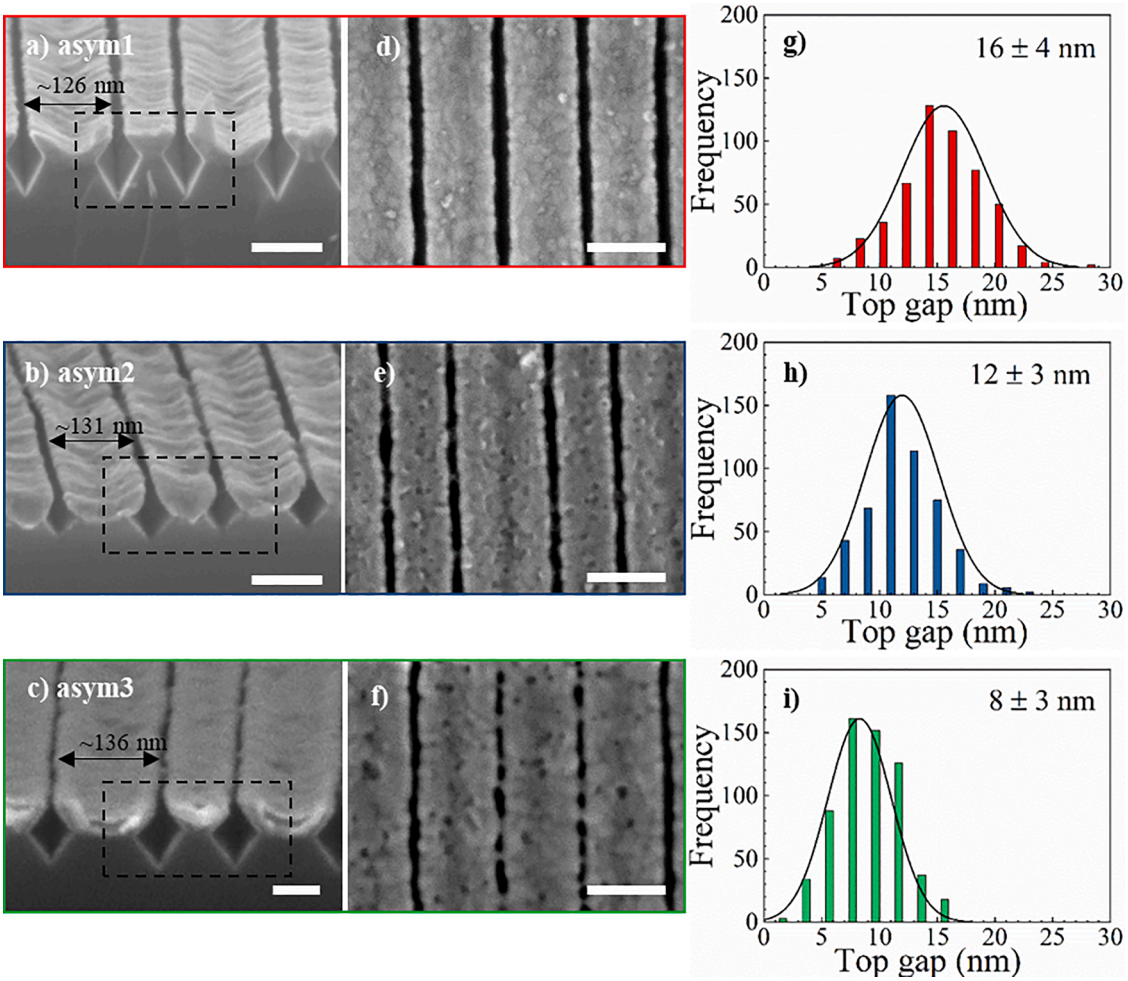

Fig. 5. (a-c) Top-view and (d-f) cross-sectional HR-SEM images of the asymmetric Au nanostructures around nano-wedges (asym1, asym2, asym3). The scale bar is 100 nm. The dashed black box shows the unit cells used in the simulations. (g-i) Corresponding size distribution histograms (N>500) of the gap as estimated from 10 different top-view HR-SEM images.

3.2. Effect of gap and etched silicon depth on electric field intensity distribution

The SERS enhancement has electromagnetic (EM) and/or chemical (CM) origin(s) [18]. In this section we elucidate about the SERS enhancement observed in the experiments, which is likely due to the EM field enhancement associated to plasmonic excitations. Focusing on the application of SERS-active symmetric and asymmetric Au nanogaps, we

first show by FDTD simulations that these structures may exhibit significant SERS enhancement based on the high EM field enhancements obtained from simulations. Furthermore, we discuss the possible types of plasmonic resonances supported by these structures that could explain such high enhancements.

The 3D-dimensions of the nanostructures and the dielectric constants of the materials of which they are made have a significant impact on the SERS signal. To identify potential designs for effective SERS, FDTD simulations can be used to establish specific criteria.

Firstly, we created a base simulation with a parametric symmetric Au nanogap structure model (Fig. 6a), which then was used to perform a parameter sweep with different nanogaps (*G, G* = 2–16 nm), and depths of the rhombic cross-sectional feature etched at the top of the silicon nano-wedges (*SiD*, SiD = 0–100 nm). A constant parameter in our Au nanogap model was the thickness of the overhanging Au nanostructures ("Au-nanoflaps"), which was set to 17 nm for the complete study, in accordance with the fabricated samples. After the nanogap model construction, the FDTD were configured as described in the method section.

Fig. 6b shows the enhancement of the electric field intensity in the gap (averaged in a small nearby region, black box of Fig. 6c) as a function of the wavelength, for different etched silicon depths (gap of 6 nm). The spectral window investigated shows a clear resonance for each silicon depth, which develops from a low broadband peak at lower etching depths to a strong and narrow resonance around SiD ~ 40 nm. As the etched depth increases further, the resonance intensity starts to diminish again.

The nanostructured systems studied can be viewed as subwavelength metallic gratings composed of slits. The study of slit arrays on metals has been extensively researched in relation to Extraordinary Optical Transmission phenomena [51]. The slits are usually carved into flat metal surfaces, which makes them more convenient for theoretical analysis. Although the SERS nanostructures fabricated here are much more complex than flat metal films corrugated with slits, they share most of the optical features displayed by them, as shown hereafter. Slit arrays are highly sensitive to the polarization of incident light, with their most notable effect being that resonances are only observable when the electric field is perpendicular to the invariant direction (*y*-direction) [52]. This has important consequences on the SERS effect formation, as we demonstrate in the next section.

Slit arrays support two different types of plasmonic resonances, originating either from Surface Plasmon Polaritons (SPPs) or Localized Plasmon Polaritons (LSPs) [51]. The first have been related to excitations of resonances in the optical spectrum of optically thick films (thicknesses > skin-depth of the metal) at wavelengths slightly above the condition $\lambda_R \sim n \times p$ (where p is the lattice constant, n the refractive index of the substrate and R states for resonant). For films that are optically thin, the surface resonances may experience significant redshifts [53]. The second type of plasmonic resonances are Fabry-Perot modes, which depend on the optical path of light inside the slits [51]. In plasmonic structures, these resonances are also dependent on the phase change that occurs upon reflection at the cavity's end, defined by the slits. Our SERS nanostructures are optically thin, such that we can safely neglect the first effect (SPPs resonances) [52].

We elucidate that the main parameter controlling the position and shape of the resonances in Fig. 6b is the phase change, which depend on the dielectric environment around the nanogaps. However, surface plasmonic effects cannot be disregarded. As we will show later, without removal the Cr layer strongly impairs the resonant response of the system. Therefore, it is possible that hybridization could occur between localized and surface modes, as SPP resonances are expected to occur at wavelengths greater than $n \times p \sim 3.83 \times 120 = 460nm$. The etched silicon depth, SiD, affects both modes. When SiD increases, the resonance shifts to shorter wavelengths, which is caused by the metal "seeing" a lower refractive index, as illustrated in Fig. 6b.

Another shared feature between flat metal slits and our Au nanostructures is the similar field distribution of light inside the gap [51]. Fig. 6c displays the distribution of normalized electrical field intensity for a nanostructure with an etched silicon depth of SiD = 39 nm and a

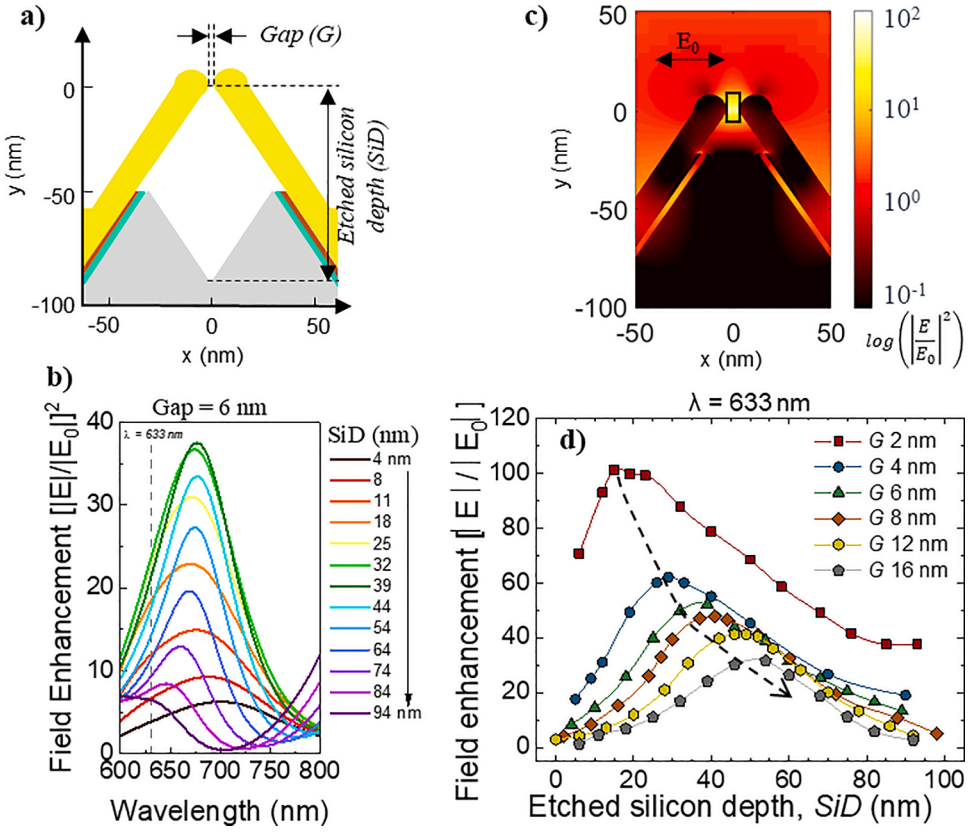

Fig. 6. (a) Schematic side view of the nano-wedge-based symmetric Au nanostructure model for FDTD simulations. color code: gray, Si; blue, SiO_2; orange, Cr; yellow, Au. (b) Intensity of the electric field enhancement as a function of the wavelength, for different etched silicon depths (SiD) (the gap, G, fixed at 6 nm). The system is illuminated from the air side or topside from the positive y-direction at normal incidence. The incident electric field is pointing perpendicular to the gap (x-direction). (c) Color-coded FDTD-simulated image of the electric field intensity distribution for a gap of 6 nm and an etched SiD of 39 nm at the wavelength with the maximum of intensity enhancement shown in panel b) at λ = 680 nm; (d) FDTD-simulated electromagnetic field enhancement averaged over the gap region (black box of c)) versus etched silicon depth for six different gaps. The gray dashed line shows the trend of the maximum field enhancement as a function of G and SiD for λ = 633 nm.

nanogap of $G = 6$ nm. The near-field map corresponds to the maximum point on the intensity enhancement curve shown in Fig. 6b (at a wavelength of 680 nm). The electric field points from side to side inside the gap (*x*-direction), which in the study of slit arrays is attributed to the excitation of TEM modes [51]. These modes have no cutoff, so light can always propagate inside the slits, which at the Fabry-Perot resonance condition makes the existence of strong peaks in the transmission spectrum of a slit array possible.

Fig. 6d shows the average electric field intensity enhancement in the gap region (black box of Fig. 6c), obtained for the region between the gap boundaries, as a function of *SiD* (calculated for six different gap values) at the laser wavelength used in this work, at 633 nm. This wavelength is indicated in Fig. 6b with a vertical dashed line. Given the evolution of the resonance as a function of *SiD*, we expect such a variation in the averaged intensity enhancement. The results in Fig. 6d show that the enhancement features a different maximum value per *SiD*, and strongly depends on the nanogap size *G*. Narrowing the gap results in higher valued of the maximum local field enhancement factor ($(E/E_0)^2$), as could be expected [23]. A parameter sweep of *SiD* shows the existence of an optimum *SiD* value that maximizes the local field enhancement factor $(E/E_0)^2$. The found optimum *SiD* values depend on the *G* values and are in the range of 20 to 60 nm, for the simulations considered in this study (Fig. 6d).

Finally, it is worth to discuss the effects of absorption in the Si substrate and the presence of Cr in the SERS nanostructures. Fig. 7a shows the EM field enhancement over the gap region as a function of etched silicon depth for three different SERS nanostructures with a gap size of 6 nm. The three structures were characterized by the presence or absence of a Cr layer and the use of the real or complex part of the dielectric constant of Si in the calculations. The dominant role of Si in the optical response of the system is due to its high real part value of dielectric constant, as observed in Fig. 7a: Si without imaginary part of the dielectric constant (i.e., transparent material) produces a similar optical response to that of Si with damping.

Absence of the Cr layer introduces an interesting dependence, a sort of plateau for large values of the etched silicon depth. This optical response comes from the reduction of the absorption after removing the Cr layer. Cr is considered as a poor metal in plasmonic gratings because it strongly absorbs the field components of localized and surface plasmons [54]. Removing the Cr layer from the system in Fig. 6b results in narrower and more intense resonances (Fig. 7b), particularly at lower wavelengths where the absorption of Cr is higher.

3.3. Experimental results of symmetric and asymmetric Au nanogaps on nano-wedges

Essential requirements for SERS substrate are large-scale homogeneity of the width of the nanogap, reproducibility during nanofabrication and uniform SERS signal intensity [15,55]. These parameters are assessed by means of the evaluation of SERS activity at three different locations on the same SERS substrate. The recorded measurements were performed over three areas of 50 μm × 50 μm measuring 100 spectra (examples of these mappings are shown in Figs 8a-8b). These kinds of measurements, i.e., SERS mappings, provide a robust methodology for SERS analysis [55].

Fig. 8c shows SERS spectra of R6G that were acquired, under identical experimental conditions, for the different specimens with symmetric Au nanogaps. In accordance with FDTD simulations, measurements on symmetrical nanogaps of the SERS signal of R6G exhibited a dependence on the etched silicon depth. In the case of the specimen with symmetric Au nanostructures with a gap of ~ 6 nm, the SERS intensity increased for a larger etched silicon depth. It has to be noted that the RSD of the SERS intensities were 9%, 38%, and 11% for symmetric Au nanogaps templated over silicon with depths of 0 nm (sym1), ~ 13 nm (sym2) and ~ 40 nm (sym3), respectively. In addition, when the SiO_2 support and the metallic Cr layer used as the adhesion layer remained underneath the Au nanoflaps (substrate sym4), the SERS intensity decreased. In this last case, the RSD was 15%. Fig. S2 shows the experimental and theoretical SERS enhancement: the presence of Cr causes a reduction of the SERS intensity due to plasmon coupling losses introduced by the Cr [56–58]. Identical beneficial results have also been reported for silver-capped silicon nanopillars upon removal of the chromium layer [59].

In the case of asymmetric Au nanostructures, as shown in Fig. 8d, reduction of the gap resulted in an increase of the SERS intensity: the asymmetric Au specimen with the smallest gap (~8 nm) exhibited a response with a significantly higher SERS intensity than the specimen with larger gaps. It has to be noted that the standard deviations of the SERS intensities recorded on asymmetric Au nanostructures with gaps of ~16 nm, ~12 nm, and ~8 nm, were 21%, 30%, and 30%, respectively. The relatively low uniformity of the SERS activity for these small gaps could be attributed to the variation of the size of the gap. For an average gap of 8 nm, variations of 1 nm could greatly change the SERS intensity because the electric field amplitude shows an approximate inverse dependence with the gap size [18].

From averaging the mapping results, the analytical enhancement factor (AEF) was calculated using Eq. (1) and the results are shown in Fig. 9. It is worth mentioning that the theoretical SERS electromagnetic enhancement factor is approximately described by Eq. (2) [18]:

$$EF \propto \left[\frac{|E|}{|E_0|}\right]^4 \tag{2}$$

Where |E| is the amplitude of the enhanced electric field in the gap re-

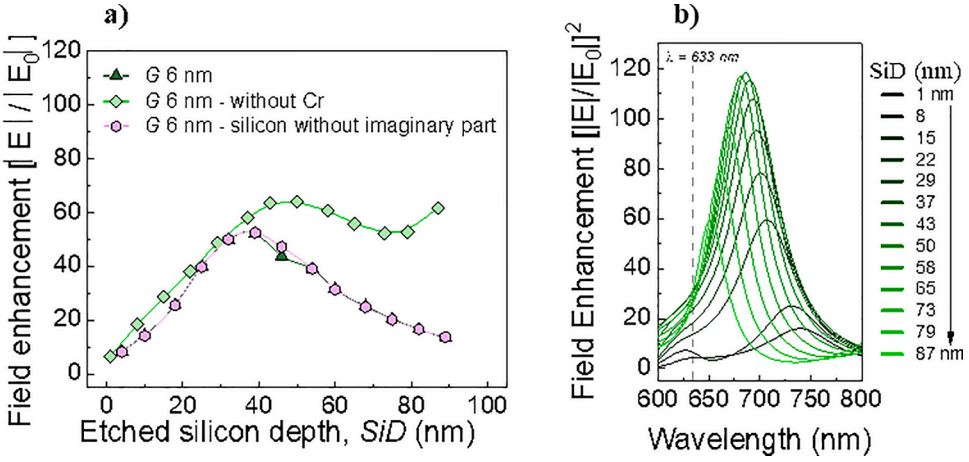

Fig. 7. (a) FDTD-simulated electromagnetic field enhancement averaged over the gap region versus etched silicon depth for $G = 6$ nm for three different SERS nanostructures: (triangles) the Cr layer is present and the Si layer absorbs the light; (diamonds) the Cr layer is removed (Si still absorbs); (hexagons); the Cr layer is present but only the real part of the dielectric constant of Si is considered in calculations (the substrate is transparent). (b) Electric field intensity enhancement as a function of the wavelength, for different etched silicon depths (SiD) (the gap, G, is set to 6 nm). The Cr layer has been removed in the calculations. The system is illuminated from the air side at normal incidence. The incident electric field is pointing perpendicular to the gap.

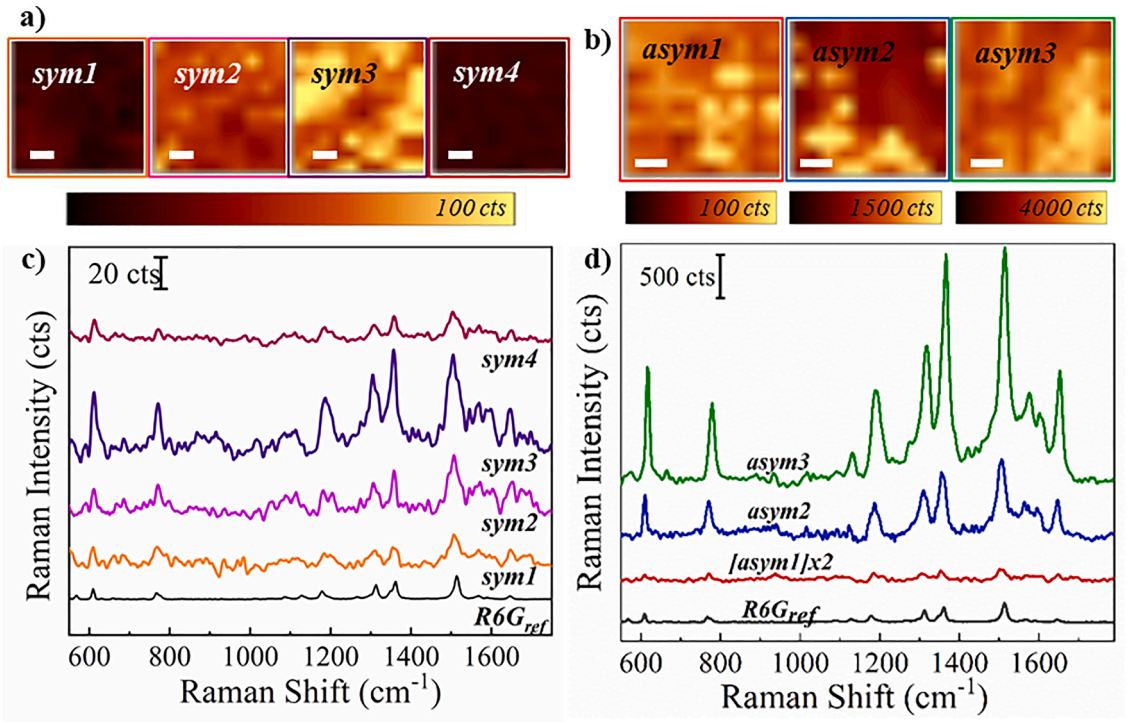

Fig. 8. a)-b) SERS mappings (50 × 50 μm, 100 spectra) monitoring peak at 1510 cm^{-1} of R6G for a) symmetric and b) asymmetric nanostructures. The scale bar represents 10 μm. c)-d) The average SERS spectra of R6G 1 μM obtained on these SERS mappings as well as with the Raman spectrum of pure R6G in solid phase. Each spectrum is the average of 100 spectra. For better interpretation of the results SERS spectra are displayed with an offset in the y-direction.

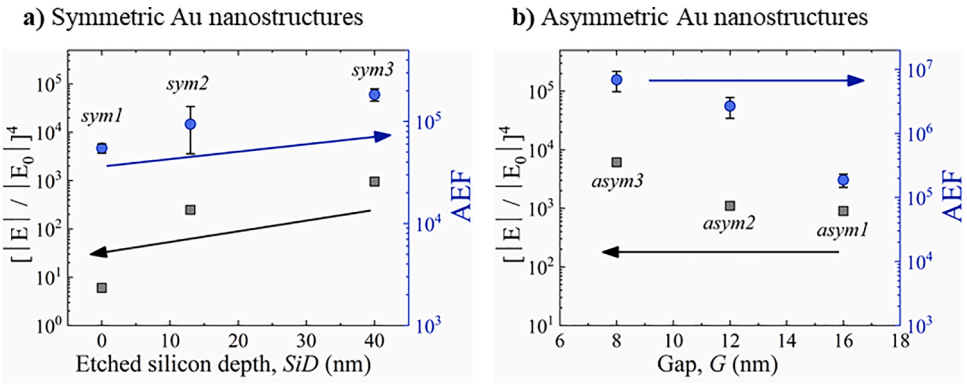

Fig. 9. (a) Effect of SiD on SERS enhancement: theoretical (black) and experimental (blue) SERS enhancement results of specimen with symmetric Au nanostructures with different SiD-values: 0, 13 and 40 nm. (b) Effect of G on SERS enhancement: theoretical (black) and experimental (blue) SERS enhancement results of specimen with asymmetric Au nanostructures with different G-values: 8, 12 and 16 nm. The error bars indicate standard deviation.

gion and $|E_0|$ is the amplitude of the incoming electromagnetic wave.

As can be seen in Fig. 9b (see also Figure S3 in SI), the asymmetric Au nanostructures show a better SERS response than the symmetric specimen (Fig. 9a), where asym3 achieved an AEF of 6.9 × 10^6. In addition, we can observe that the experimental AEF is about a factor ~10^2 - 10^3 larger than the theoretical EM SERS enhancement calculated with Eq. (2), nevertheless, both the theoretical and experimental EM SERS enhancement factors follow the same relative trend, which supports the validity of the FDTD simulations. The discrepancy between the measured and calculated EM SERS enhancements arises from a varieties aspect that include differences between experimental samples and the theoretical models (e.g. dimensional imperfections of the samples, slightly different dielectric constants of materials, etc.) that eventually result in the fact that resonances appear at different spectral locations. Another important source of discrepancies is that we used an approach based on a simple expression of the SERS signal (Eq. (2)). It is well known that this expression is able to predict qualitative trends of SERS but not quantitative results.

Finally, the polarization effect has been verified experimentally from SERS signals in asymmetric structures (see SEM images in Fig. 10). In the experiments, the incoming light was polarized parallel and perpendicular to the width-direction of the Au nanostructures (Fig. 10a). The results showed that the Raman signals of R6G for two polarization directions differ by almost a factor of 5 for asym1 and 10 for asym2, by being higher for the E_0 parallel-orientation to the width of the Au nanostructure (see Fig. 10b). In other words, in our experiments, the largest Raman enhancement was found for light perpendicularly oriented to the width gap.

From the experimental and theoretical approaches, we can now narrow the selection of the best performing SERS substrate. The asymmetric Au nanogaps are found to yield a better SERS response than the symmetric nanogaps. The highest SERS enhancement of 6.9 × 10^6 is

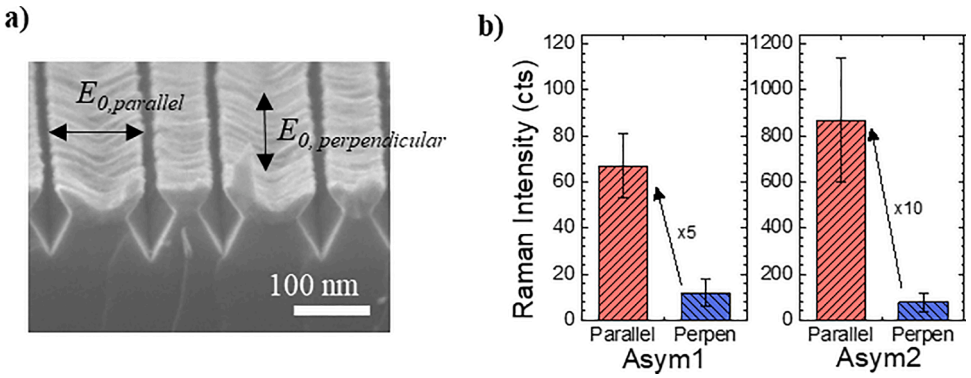

Fig. 10. a) Scheme indicating the direction of light polarized in parallel and perpendicular to the width-direction of the gold nanostructures or gap width. b) The average SERS intensity of the peak at 1510 cm^{-1} of R6G 1 μM recorded on samples 'asym1'and 'asym2' with the incoming laser light polarized parallel and perpendicular to the width-direction of the gold nanostructures.

achieved with specimen asym3.

Conclusions

We have fabricated symmetric and asymmetric Au gaps templated over silicon nano-wedges. The nano-wedges were realized by a combination of displacement Talbot lithography (DTL), corner lithography and selective anisotropic etching of silicon. Subsequently, Au nanogaps were formed on the nano-wedges by means of ion beam etching (IBE) of sputter-deposited Au (Au) films. The thickness of the sputtered Au film determined the nanogap type: Symmetric or asymmetric, and the time of IBE the width of the Au nanogap. The gap dimensions in-between the Au nanostructures surrounding the tip of nano-wedges, and thus the hot-spot formation, was highly tuneable by means of the silicon depth of the rhombic cage and by varying the thickness of the secondary sputtered Au layer. This was demonstrated by varying gap width from 2 to 16 nm while varying rhombic cage depth from 0 to 100 nm. This novel fabrication protocol resulted in robust and uniform SERS specimen, with very well controlled gaps in the range of 6 ± 2 nm to 16 nm ± 4 nm. We have firstly analyzed the SERS activity of these symmetric and asymmetric Au nanostructures by FDTD simulations. In the case of symmetric Au nanogaps, the SERS effects arise mainly at the gap between the Au nanoflaps. For both symmetric as well as asymmetric Au nanostructures upon reduction of the gap, the enhanced electric field increases. In addition, for asymmetric Au nanostructures the electric field enhancement is the highest close to the Au nanostructure with the largest cross-sectional. It shows that the Raman enhancement depends on the orientation of the light polarization with respect to the width direction of the Au nanogaps. Theoretically predicted designs for more active SERS nanostructures agree with the experimental tendencies shown by the fabricated specimens with R6G. The exhibited AEF values are paving the way for future developments where SERS is combined with sieving effect at the nanogaps.

Author contributions

M.L.: conceptualization, methodology, software, investigation, data curation, writing the original draft and editing the manuscript. P.M.: methodology and software. E.J.W.B.: methodology and validation. R.M. T.: writing – review and editing, supervision. A.S-A.: writing – review and editing. S.G.R.: investigation, validation, data curation and writing. L.J.K.: data curation and writing. S.M.G-B.: review and funding acquisition. R.M.: original idea, review, supervision and funding acquisition. M.P.P.: original idea, review, supervision and funding acquisition. N.R. T.: original idea, review, supervision and funding acquisition. All authors have given approval to the final version of the manuscript.

Funding sources

S.G.R., R.M. and M.P.P are grateful for financial support from: the European Union's Horizon 2020 research and innovation program under grant agreement No. 883390 (H2020-SU-SECU-2019 SERSing Project) and R.M and M.P.P for financial support from AEI Spain (PID2019-108660RB-I00). P.M. and S.M.G.B thanks funding by the Dutch Research Council (contract number 13328).

Declaration of Competing Interest

The authors declare that they have no known competing financial interests or personal relationships that could have appeared to influence the work reported in this paper.

Data availability

Data will be made available on request.

Supplementary materials

Supplementary material associated with this article can be found, in the online version, at doi:10.1016/j.apmt.2023.101929.

References

[1] D.C. Harris, M.D. Bertolucci, Symmetry and spectroscopy: an Introduction to Vibrational and Electronical Spectroscopy, Dover Publications, New York, 1978.
[2] R.A. Alvarez-Puebla, A. Agarwal, P. Manna, B.P. Khanal, P. Aldeanueva-Potel, E. Carbo-Argibay, N. Pazos-Perez, L. Vigderman, E.R. Zubarev, N.A. Kotov, L. M. Liz-Marzan, Gold nanorods 3D-supercrystals as surface enhanced Raman scattering spectroscopy substrates for the rapid detection of scrambled prions, Proc. Natl Acad. Sci. 108 (2011) 8157–8161, https://doi.org/10.1073/pnas.1016530108.
[3] S. Shanmukh, L. Jones, J. Driskell, Y. Zhao, R. Dluhy, R.A. Tripp, Rapid and sensitive detection of respiratory virus molecular signatures using a silver nanorod array SERS substrate, Nano Lett. 6 (2006) 2630–2636, https://doi.org/10.1021/nl061666f.
[4] E. Garcia-Rico, R.A. Alvarez-Puebla, L. Guerrini, Direct surface-enhanced Raman scattering (SERS) spectroscopy of nucleic acids: from fundamental studies to real-life applications, Chem. Soc. Rev. (2018), https://doi.org/10.1039/C7CS00809K.
[5] C.L. Wong, U.S. Dinish, M.S. Schmidt, M. Olivo, Non-labeling multiplex surface enhanced Raman scattering (SERS) detection of volatile organic compounds (VOCs), Anal. Chim. Acta 844 (2014) 54–60, https://doi.org/10.1016/j.aca.2014.06.043.
[6] Y. Zhu, H. Kuang, L. Xu, W. Ma, C. Peng, Y. Hua, L. Wang, C. Xu, Gold nanorod assembly based approach to toxin detection by SERS, J. Mater. Chem. 22 (2012) 2387–2391, https://doi.org/10.1039/C2JM15238J.
[7] M. Lafuente, I. Pellejero, A. Clemente, M.A. Urbiztondo, R. Mallada, S. Reinoso, M. P. Pina, L.M. Gandía, In situ synthesis of SERS-active Au@POM nanostructures in a microfluidic device for real-time detection of water pollutants, ACS Appl. Mater. Interfaces 12 (2020) 36458–36467, https://doi.org/10.1021/acsami.0c06725.

[8] E. Segal, E. Haleva, A. Salomon, Ultrasensitive plasmonic sensor for detecting Sub-PPB levels of alachlor, ACS Appl. Nano Mater. 2 (2019) 1285–1293, https://doi.org/10.1021/acsanm.8b02164.

[9] A. Hakonen, K. Wu, M. Stenbæk Schmidt, P.O. Andersson, A. Boisen, T. Rindzevicius, Detecting forensic substances using commercially available SERS substrates and handheld Raman spectrometers, Talanta 189 (2018) 649–652, https://doi.org/10.1016/j.talanta.2018.07.009.

[10] S.K. Islam, Y. Pak, R.L. Birke, M. Vega, C. Muehlethaler, J.R. Lombardi, An analysis of tetrahydrocannabinol (THC) and its analogs using surface enhanced Raman Scattering (SERS), Chem. Phys. 536 (2020), 110812, https://doi.org/10.1016/j.chemphys.2020.110812.

[11] M. Lafuente, D. Sanz, M.A. Urbiztondo, J. Santamaría, M.P. Pina, R. Mallada, Gas phase detection of chemical warfare agents CWAs with portable Raman, J. Hazard. Mater. 384 (2020), 121279, https://doi.org/10.1016/j.jhazmat.2019.121279.

[12] M. Lafuente, E.J.W. Berenschot, R.M. Tiggelaar, R. Mallada, N.R. Tas, M.P. Pina, 3D fractals as SERS active platforms: preparation and evaluation for gas phase detection of G-nerve agents, Micromachines (Basel) 9 (2018), https://doi.org/10.3390/mi9020060.

[13] E.Le Ru, P.G. Etchegoin, Principles of Surface-Enhanced Raman Spectroscopy and Related Plasmonic Effects, 2009th ed., Elsevier, 2009.

[14] A. Shiohara, Y. Wang, L.M. Liz-marzán, Recent approaches toward creation of hot spots for SERS detection, J. Photochem. Photobiol., C: Photochem. Rev. 21 (2014) 2–25, https://doi.org/10.1016/j.jphotochemrev.2014.09.001.

[15] M. Fan, G.F.S. Andrade, A.G. Brolo, A review on recent advances in the applications of surface-enhanced Raman scattering in analytical chemistry, Anal. Chim. Acta 1097 (2020) 1–29, https://doi.org/10.1016/j.aca.2019.11.049.

[16] A. Susarrey-Arce, K.M. Czajkowski, I. Darmadi, S. Nilsson, I. Tanyeli, S. Alekseeva, T.J. Antosiewicz, C. Langhammer, A nanofabricated plasmonic core-shell-nanoparticle library, Nanoscale 11 (2019) 21207–21217, https://doi.org/10.1039/c9nr08097j.

[17] M. Lafuente, I. Pellejero, V. Sebastián, M.A. Urbiztondo, R. Mallada, M.P. Pina, J. Santamaría, Highly sensitive SERS quantification of organophosphorous chemical warfare agents: a major step towards the real time sensing in the gas phase, Sens. Actuat. B Chem. 267 (2018) 457–466, https://doi.org/10.1016/j.snb.2018.04.058.

[18] P.L. Stiles, J.A. Dieringer, N.C. Shah, R.P. Van Duyne, Surface-enhanced Raman spectroscopy, Annu. Rev. Anal. Chem. 1 (2008) 601–626, https://doi.org/10.1146/annurev.anchem.1.031207.112814.

[19] M. Lafuente, S. Ruiz-Rincón, R. Mallada, P. Cea, M.Pilar Pina, Towards the reproducible fabrication of homogeneous SERS substrates by Langmuir-Schaefer technique: a low cost and scalable approach for practical SERS based sensing applications, Appl. Surf. Sci. (2019), 144663, https://doi.org/10.1016/j.apsusc.2019.144663.

[20] J. Lee, B. Hua, S. Park, M. Ha, Y. Lee, Z. Fan, H. Ko, Tailoring surface plasmons of high-density gold nanostar assemblies on metal films for surface-enhanced Raman spectroscopy, Nanoscale 6 (2014) 616–623, https://doi.org/10.1039/c3nr04752k.

[21] R. Tantra, R.J.C. Brown, M.J. Milton, Strategy to improve the reproducibility of colloidal SERS, J. Raman Spectrosc. 38 (2007) 1469–1479, https://doi.org/10.1002/jrs.1797.

[22] J. Chen, L. Guo, B. Qiu, Z. Lin, T. Wang, Application of ordered nanoparticle self-assemblies in surface-enhanced spectroscopy, Mater. Chem. Front. (2018) 835–860, https://doi.org/10.1039/C7QM00557A.

[23] H. Le-The, J.J.A. Lozeman, M. Lafuente, P. Muñoz, J.G. Bomer, H. Duy-Tong, E. Berenschot, A. van den Berg, N.R. Tas, M. Odijk, J.C.T. Eijkel, Wafer-scale fabrication of high-quality tunable gold nanogap arrays for surface-enhanced Raman scattering, Nanoscale 11 (2019) 12152–12160, https://doi.org/10.1039/C9NR02215E.

[24] A. Habermehl, P. Brenner, R. Huber, A. Mertens, F. Winkler, L. Hahn, M. Guttmann, C. Eschenbaum, U. Lemmer, Roll-to-roll hot embossing of 1D and 2D photonic nanostructures, Adv. Eng. Mater. 21 (2019), 1900110, https://doi.org/10.1002/adem.201900110.

[25] T. Jiang, P. Goel, H. Zhao, R. Ma, L. Zhu, X. Liu, Internal structure tailoring in 3D nanoplasmonic metasurface for surface-enhanced Raman spectroscopy, Particle Particle Syst. Characteriz. 37 (2020) 1900345. doi:10.1002/ppsc.201900345.

[26] D. Jonker, Z. Jafari, J.P. Winczewski, C. Eyovge, J.W. Berenschot, N.R. Tas, J.G. E. Gardeniers, I. De Leon, A. Susarrey-Arce, A wafer-scale fabrication method for three-dimensional plasmonic hollow nanopillars, Nanoscale Adv. 3 (2021) 4926–4939, https://doi.org/10.1039/d1na00316j.

[27] M. Kahl, E. Voges, S. Kostrewa, C. V, W. Hill, Periodically structured metallic substrates for SERS, Sens. Actuat. B Chem. 51 (1998) 285–291, https://doi.org/10.1016/S0925-4005(98)00219-6.

[28] C.-W. Chang, J.-D. Liao, A.-L. Shiau, C.-K. Yao, Non-labeled virus detection using inverted triangular Au nano-cavities arrayed as SERS-active substrate, Sens. Actuat. B Chem. 156 (2011) 471–478, https://doi.org/10.1016/j.snb.2011.04.006.

[29] H.H. Solak, C. Dais, F. Clube, Displacement Talbot lithography: a new method for high-resolution patterning of large areas, Opt. Express 19 (2011) 10686, https://doi.org/10.1364/oe.19.010686.

[30] D. Jonker, E.J.W. Berenschot, N.R. Tas, R.M. Tiggelaar, A. Van Houselt, H.J.G. E. Gardeniers, Large dense periodic arrays of vertically aligned sharp silicon nanocones, Nanoscale Res. Lett. 17 (2022) 100, https://doi.org/10.1186/s11671-022-03735-y.

[31] D. Jonker, L. Kooijman, Y. Pordeli, B. van der Wel, E. Berenschot, B. Borgelink, H. Le-The, M. de Boer, J. Eijkel, R. Hueting, R. Tiggelaar, A. van Houselt, H. Gardeniers, N. Tas, Wafer-scale fabrication and modification of silicon nano-pillar arrays for nanoelectronics, nanofluidics and beyond, Int. J. Nanotechnol. 17 (2020) 583–606, https://doi.org/10.1504/IJNT.2020.111322.

[32] E.J.W. Berenschot, H.V. Jansen, N.R. Tas, Fabrication of 3D fractal structures using nanoscale anisotropic etching of single crystalline silicon, J. Micromech. Microeng. 23 (2013), https://doi.org/10.1088/0960-1317/23/5/055024.

[33] E. Berenschot, R.M. Tiggelaar, B. Borgelink, C. van Kampen, C.S. Deenen, Y. Pordeli, H. Witteveen, H.J.G.E. Gardeniers, N.R. Tas, Self-aligned crystallographic multiplication of nanoscale silicon wedges for high-density fabrication of 3D nanodevices, ACS Appl. Nano Mater. 5 (2022) 15847–15854, https://doi.org/10.1021/acsanm.2c04079.

[34] M. Chirumamilla, A. Toma, A. Gopalakrishnan, G. Das, R.P. Zaccaria, R. Krahne, E. Rondanina, M. Leoncini, C. Liberale, F. de Angelis, E. di Fabrizio, 3D nanostar dimers with a sub-10-nm gap for single- /few-molecule surface-enhanced Raman scattering, Adv. Mater. 26 (2014) 2353–2358, https://doi.org/10.1002/adma.201304553.

[35] M. Tabatabaei, M. Najiminaini, K. Davieau, B. Kaminska, M.R. Singh, J.J.L. Carson, F. Lagugné-Labarthet, Tunable 3D plasmonic cavity nanosensors for surface-enhanced Raman spectroscopy with sub-femtomolar limit of detection, ACS Photonics 2 (2015) 752–759, https://doi.org/10.1021/acsphotonics.5b00104.

[36] A. Gopalakrishnan, M. Chirumamilla, F. de Angelis, A. Toma, R. Proietti Zaccaria, R. Krahne, Bimetallic 3D nanostar dimers in ring cavities: recyclable and robust surface-enhanced Raman scattering substrates for signal detection from few molecules, ACS Nano 8 (2014) 7986–7994, https://doi.org/10.1021/nn5020038.

[37] H.I. Smith, R. Menon, A. Patel, D. Chao, M. Walsh, G. Barbastathis, Zone-plate-array lithography: a low-cost complement or competitor to scanning-electron-beam lithography, Microelectron. Eng. 83 (2006) 956–961, https://doi.org/10.1016/j.mee.2006.01.226.

[38] X. Zhang, W.J. Salcedo, M.M. Rahman, A.G. Brolo, Surface-enhanced Raman scattering from bowtie nanoaperture arrays, Surf. Sci. 676 (2018) 39–45, https://doi.org/10.1016/j.susc.2018.02.003.

[39] A. Ahmed, R. Gordon, Single molecule directivity enhanced Raman scattering using nanoantennas, Nano Lett. 12 (2012) 2625–2630, https://doi.org/10.1021/nl301029e.

[40] Q. Tao, S. Li, C. Ma, K. Liu, Q.Y. Zhang, A highly sensitive and recyclable SERS substrate based on Ag-nanoparticle-decorated ZnO nanoflowers in ordered arrays, Dalton Trans. 44 (2015) 3447–3453, https://doi.org/10.1039/C4DT03596H.

[41] Q. Zhang, Y.H. Lee, I.Y. Phang, C.K. Lee, X.Y. Ling, Hierarchical 3D SERS substrates fabricated by integrating photolithographic microstructures and self-assembly of silver nanoparticles, Small 10 (2014) 2703–2711, https://doi.org/10.1002/smll.201303773.

[42] S. Yan, F. Chu, H. Zhang, Y. Yuan, Y. Huang, A. Liu, S. Wang, W. Li, S. Li, W. Wen, Rapid, one-step preparation of SERS substrate in microfluidic channel for detection of molecules and heavy metal ions, Spectrochim. Acta A Mol. Biomol. Spectrosc. 220 (2019), 117113, https://doi.org/10.1016/j.saa.2019.05.018.

[43] M.S. Schmidt, J. Hübner, A. Boisen, Large area fabrication of leaning silicon nanopillars for surface enhanced Raman spectroscopy, Adv. Mater. 24 (2012) 11–18, https://doi.org/10.1002/adma.201103496.

[44] H. Le-The, E. Berenschot, R.M. Tiggelaar, N.R. Tas, A. van den Berg, J.C.T. Eijkel, Shrinkage control of photoresist for large-area fabrication of sub-30nm periodic nanocolumns, Adv. Mater. Technol. 2 (2017), https://doi.org/10.1002/admt.201600238.

[45] H. Le-The, R.M. Tiggelaar, E. Berenschot, A. Van Den Berg, N. Tas, J.C.T. Eijkel, Postdeposition UV-ozone treatment: an enabling technique to enhance the direct adhesion of gold thin films to oxidized silicon, ACS Nano 13 (2019) 6782–6789, https://doi.org/10.1021/acsnano.9b01403.

[46] J.G.E. Wilbers, J.W. Berenschot, R.M. Tiggelaar, T. Dogan, K. Sugimura, W.G. Van Der Wiel, J.G.E. Gardeniers, N.R. Tas, 3D-fabrication of tunable and high-density arrays of crystalline silicon nanostructures, J. Micromech. Microeng. 28 (2018), https://doi.org/10.1088/1361-6439/aaab2d.

[47] E.D. Palik, Handbook of Optical Constants of Solids, Academic press, 1998. Volume III.

[48] W.M. Haynes, CRC handbook of chemistry and physics, 95th Editi, 2014.

[49] E.C. Le Ru, E. Blackie, M. Meyer, P.G. Etchegoint, Surface enhanced Raman scattering enhancement factors: a comprehensive study, J. Phys. Chem. C 111 (2007) 13794–13803, https://doi.org/10.1021/jp0687908.

[50] R.B. Marcus, T.T. Sheng, The oxidation of shaped silicon surfaces, J. Electrochem. Soc. 129 (1982) 1278–1282, https://doi.org/10.1149/1.2124118.

[51] F.J. Garcia-Vidal, L. Martin-Moreno, T.W. Ebbesen, L. Kuipers, Light passing through subwavelength apertures, Rev. Mod. Phys. 82 (2010) 789, https://doi.org/10.1103/RevModPhys.82.729.

[52] Y. Pang, C. Genet, T.W. Ebbesen, Optical transmission through subwavelength slit apertures in metallic films, Opt. Commun. 280 (2007) 10–15, https://doi.org/10.1016/j.optcom.2007.07.063.

[53] S.G. Rodrigo, L. Martín-Moreno, A.Yu. Nikitin, A.V. Kats, I.S. Spevak, F.J. Garcia-Vidal, Extraordinary optical transmission through hole arrays in optically thin metal films, Opt. Lett. 34 (2009) 4–6.

[54] S.G. Rodrigo, F.J. García-Vidal, L. Martín-Moreno, Influence of material properties on extraordinary optical transmission through hole arrays, Phys. Rev. B Condens. Matter Mater. Phys. 77 (2008) 1–8, https://doi.org/10.1103/PhysRevB.77.075401.

[55] J. Langer, D. Jimenez de Aberasturi, J. Aizpurua, R.A. Alvarez-Puebla, B. Auguié, J. J. Baumberg, G.C. Bazan, S.E.J. Bell, A. Boisen, A.G. Brolo, J. Choo, D. Cialla-May, V. Deckert, L. Fabris, K. Faulds, F.J. García de Abajo, R. Goodacre, D. Graham, A. J. Haes, C.L. Haynes, C. Huck, T. Itoh, M. Käll, J. Kneipp, N.A. Kotov, H. Kuang, E. C. Le Ru, H.K. Lee, J.F. Li, X.Y. Ling, S.A. Maier, T. Mayerhöfer, M. Moskovits, K. Murakoshi, J.M. Nam, S. Nie, Y. Ozaki, I. Pastoriza-Santos, J. Perez-Juste, J. Popp, A. Pucci, S. Reich, B. Ren, G.C. Schatz, T. Shegai, S. Schlücker, L.L. Tay, K. G. Thomas, Z.Q. Tian, R.P. Van Duyne, T. Vo-Dinh, Y. Wang, K.A. Willets, C. Xu,

H. Xu, Y. Xu, Y.S. Yamamoto, B. Zhao, L.M. Liz-Marzán, Present and future of surface-enhanced Raman scattering, ACS Nano 14 (2019) 28–117, https://doi.org/10.1021/acsnano.9b04224.

[56] J. Liu, H. Cai, L. Kong, X. Zhu, Effect of chromium interlayer thickness on optical properties of Au-Ag nanoparticle array, J. Nanomater. 2014 (2014), 650359, https://doi.org/10.1155/2014/650359.

[57] C. Chow, J.A. Bain, Effect of thin Cr and Cu adhesion layers on surface plasmon resonance at Au/SiO2 interfaces, IEEE Trans. Magn. 52 (2016) 1–4, https://doi.org/10.1109/TMAG.2015.2509252.

[58] D.T. Debu, P.K. Ghosh, D. French, J.B. Herzog, Surface plasmon damping effects due to Ti adhesion layer in individual gold nanodisks, Opt Mater. Express 7 (2017) 73–84, https://doi.org/10.1364/OME.7.000073.

[59] K. Wu, T. Rindzevicius, M. Stenbæk Schmidt, K.B. Mogensen, A. Hakonen, A. Boisen, Wafer-scale leaning silver nanopillars for molecular detection at ultra-low concentrations, J. Phys. Chem. C 119 (2015) 2053–2062, https://doi.org/10.1021/jp510073y.